Article

Crystal Structure, Thermal Expansion and Luminescence of $Ca_{10.5−x}Ni_x(VO_4)_7$

Houri S. Rahimi Mosafer [1],*[iD], Wojciech Paszkowicz [1],*[iD], Roman Minikayev [1][iD], Christine Martin [2][iD], Mirosław Kozłowski [3], Oksana Chukova [4,5][iD], Yaroslav Zhydachevskyy [1,6][iD] and Serhii Nedilko [4][iD]

1   Institute of Physics, Polish Academy of Sciences, al. Lotnikow 32/46, 02-668 Warsaw, Poland
2   Laboratoire CRISMAT, Normandie Université, ENSICAEN, UNICAEN, CNRS, 14050 Caen, France; christine.martin@ensicaen.fr
3   Lukasiewicz Research Network, Tele- and Radio Research Institute, Ratuszowa 11, 03-450 Warsaw, Poland; miroslaw.kozlowski@itr.lukasiewicz.gov.pl
4   Faculty of Physics, Taras Shevchenko National University of Kyiv, Volodymyrska Str. 64/13, 01601 Kyiv, Ukraine; oksana.chukova@ukr.net (O.C.)
5   Deutsches Elektronen-Synchrotron (DESY), Notkestr. 85, 22607 Hamburg, Germany
6   Department of Physics and Methods of Teaching Physics, Berdyansk State Pedagogical University, 71100 Berdyansk, Ukraine
*   Correspondence: rahimi@ifpan.edu.pl (H.S.R.M.); paszk@ifpan.edu.pl (W.P.); Tel.: +48-221163301 (H.S.R.M.)

Abstract: The structural and luminescence properties of a new material, $Ca_{10.5−x}Ni_x(VO_4)_7$, formed by substitution of a fraction of calcium by nickel, are studied as a function of the Ni content (x). The powder X-ray diffraction results for the polycrystals, synthesized using a solid-state reaction method, show that in the studied temperature range (300–1150 K), the structure of the unsubstituted material (space group $R3c$, whitlockite-β-$Ca_3(PO_4)_2$ structure type) is conserved up to the solubility limit, $x = 0.72(2)$, determined on the basis of variation of unit cell size with x. The samples of nominal composition exceeding this limit contain a significant amount of the impurity phase.The structural refinements demonstrate that Ni atoms preferentially occupy the M5 site (one of the five independent Ca sites, M1–M5). The unit cell size was equally studied in the range of 300–1150 K, leading to the determination of the thermal expansion coefficients. It was found that with rising Ni content, the room temperature volumetric thermal expansion decreases from 41.80 $MK^{−1}$ ($x = 0.16$) to 39.24 $MK^{−1}$ ($x = 0.66$) and to 38.92 $MK^{−1}$ at the solubility limit, this reduction being in line with earlier reported data for x=0. In the unit cell variation, around 800–900 K, a weak anomaly is observed, detectable most clearly for the axial ratio; it is also visible at thermal expansion coefficient temperature dependence. Substitution of Ca by Ni ions reduces the optical band gap of $Ca_{10.5−x}Ni_x(VO_4)_7$ from 3.56 ($x = 0$) to 3.29 and 3.16 eV observed for Ni-containing samples ($x = 0.33$ and 0.66, respectively). Observed bands in the absorption and photoluminescence spectra are assigned to electronic transitions in both $VO_4^{3−}$ groups and Ni^{2+} ions, confirming that Ni mainly occupies the M5 site. The band gap narrowing and decrease in photoluminescence intensity when the Ni concentration increases makes Ni-substituted compounds attractive for application, e.g., as photocatalysts.

Keywords: nickel; orthovanadate; thermal expansion; structure; optical band gap; solid solution; solubility

1. Introduction

The structure of calcium orthovanadate $Ca_3(VO_4)_2$ (TCV) under ambient-conditions was first reported by Gopal and Calvo in 1973 [1], additional information can be found in [2,3] about its polymorphs formed under high-pressure. Like β-$Ca_3(PO_4)_2$ (TCP) [4], this material crystallizes in a trigonal structure corresponding to the $R3c$ space group; the reported unit cell parameters are $a = 10.809(1)$ Å and $c = 38.028(9)$ Å [1]. There are five crystallographic sites for Ca^{2+} (M1–M5), three sites for V^{5+} (V1–V3) and ten sites for $O^{2−}$

(O1–O10) [1,4,5], as illustrated in Figure 1. The M1–M5 sites differ in coordination number (CN) with oxygen atoms: M1, M2 and M3, centres of three irregular polyhedra, display 7-fold, 8-fold and 9-fold coordination, respectively. The M5 site (CN = 6) shows a regular octahedral geometry. The M4 site (CN = 3 + 3) exhibits a distinctive triangular coordination with three identical Ca–O distances, while the distances to the three other neighbouring oxygen atoms are notably longer. The cation-centred polyhedra are located in columns usually named "A" and "B" that are parallel to the c-axis [4,5]. Column B is more densely occupied compared to column A. Vanadium atoms are located on three crystallographic sites V1 (in column A), V2 and V3 (in column B). All V atoms are four-fold coordinated with oxygen atoms. An unusual characteristic of the calcium orthovanadate family is their possibility to distribute monovalent, divalent or trivalent cations (with a reported substitution rate of approximately 10 at.% of Ca atoms) on the M1–M5 crystallographic sites, while maintaining the original structure. For the substituted compounds, with full or partial occupation of specific sites, disparate chemical formulas are used, depending on the valence of the substituting element, as described in [6]. Various whitlockite-β-Ca$_3$(PO$_4$)$_2$-type compounds based on TCV can be classified as substitutionally disordered due to the mixed occupation of at least one site by calcium and foreign cations.
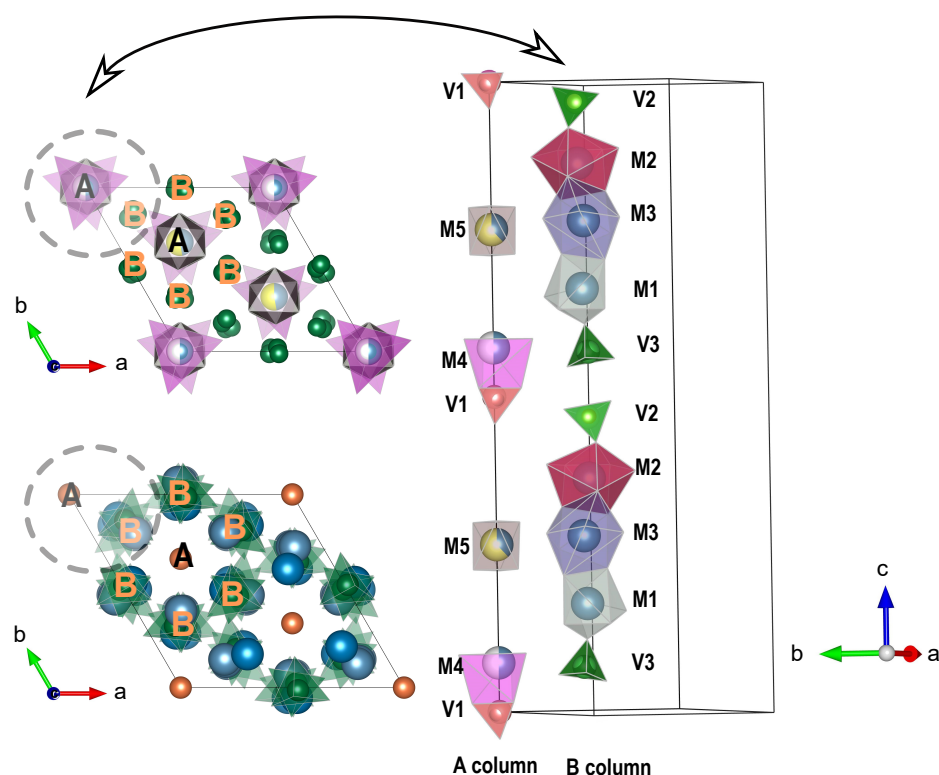
Figure 1. Two *ab*-projections of the TCV unit cell (left) highlighting the A and B columns along c that are shown on the right. The orange circles represent the vanadium centred V1, and the green circles represent V2 and V3 tetrahedra, and the blue circles show the calcium atoms located at the M1–M5 sites. The M4 site is half empty (represented by the half empty symbol), and the half blue color represents occupation by Ca ions. The blue and yellow colors at the M5 site represent Ca ions and a transition metals and Ca ions, respectively.

Most previous investigations of substituted materials of this kind have concentrated on the characterization of TCP substituted with monovalent, divalent, and trivalent cations. Studies have been conducted to substitute transition metals, zinc and magnesium into TCP, namely for Ca$_{10.5-x}$Cu$_x$(PO$_4$)$_7$ [7,8], Ca$_{10.5-x}$Co$_x$(PO$_4$)$_7$ [9–11], Ca$_9$CoM(PO$_4$)$_7$ (M = Li, Na, K) [12], Ca$_{2.90}$(Me)$_{0.10}$(PO$_4$)$_2$ (Me = Mn, Ni, Cu) [13], Ca$_{3-x}$Zn$_x$(PO$_4$)$_2$ [14], and Ca$_{3-x}$Mg$_x$(PO$_4$)$_2$ [15]. Recently, for the latter (known for a long time), using the

$Ca_9(Ca_{0.5}\square_{0.5})Mg(PO_4)_7$ formula, a new mineral name, keplerite, was introduced by the International Mineralogical Association (IMA) [16].

In contrast to orthophosphates, the knowledge of structures and applications of calcium orthovanadates substituted by monovalent and divalent ions require more investigation. Various studies on the structure and application on TCV with substitution of trivalent ions can be found in [17–22]. Only a few works concerning the substitution of TCVs with monovalent and divalent ions have been reported but they show the persistent interest in these materials. For instance, the structural analysis of $Ca_{10}K(VO_4)_7$ was studied in [23]. Subsequently, the structure of $Ca_{10}Li(VO_4)_7$, synthesized using the Czochralski method, was characterized in [24]. The Raman spectra of $Ca_{10}Na(VO_4)_7$ were analysed, but no information was provided about the structure of this material [25]. High-temperature diffusion methods to prepare Mn-doped $Ca_3(VO_4)_2$ single crystals was reported in [26]. Very recently, the effect of cobalt doping of $Ca_3(VO_4)_2$ single crystal was investigated using X-ray diffraction and absorption spectroscopy: the formal charge of cobalt, between 2+ and 3+, is found to decrease when increasing the Co concentration [27]. The structural impact of Cu and Co substitution into $Ca_3(VO_4)_2$ ($Ca_{10}Cu_{0.5}(VO_4)_7$, $Ca_{10}Co_{0.5}(VO_4)_7$) studied at room and high temperature demonstrates that cobalt and copper occupy the M5 site [6]. Even though Ni belongs to the same row of the Periodic Table as Mn, Co, and Cu, there is currently a lack of data regarding the structure and peculiarities of yet unreported Ni^{2+} ion incorporation into the $Ca_3(VO_4)_2$ crystal and the influence on its properties.

Unsubstituted and substituted variants of $Ca_3(VO_4)_2$, among other compounds, exhibit diverse and valuable properties. Notably, $Ca_3(VO_4)_2$ demonstrates a remarkably high Curie temperature (T_c = 1383 K) and is the first reported ferroelectric in the whole TCV family, rendering it a significant and fascinating material [28]. This crystal possesses non-linear optical properties [29]. Orthovanadates present intrinsic photoluminescence (PL) relating to the VO_4^{3-} groups [30–32]. Furthermore, they are well-known matrices for luminescent rare-earth (RE) ion doping, enhancing the PL characteristics [33–35] and making the material attractive for white LED applications [36,37]. Substituting and co-doping $Ca_3(VO_4)_2$ with M^+, M^{2+}, M^{3+}, and RE^{3+} ions also improves the optical properties [37,38]. Particularly, the nickel ions in the composition of vanadates increase their abilities in photocatalysis [39,40], accumulator cells cathode and anode electrodes [41], energy storage devices [42], and solar-driven photo-electrochemical water oxidation [43]. The above-mentioned applications require knowledge of the effect of Ni ions on not only the structural components of the crystal lattice, but also the behaviour of the band gap and photo-excited electronic energy. The band gap energy can be estimated from the optical absorption spectra, but there are limited reports concerning this value for TCV families. The direct band gap of $Ca_3(VO_4)_2$ was found to be 3.55 eV [44]. The band gap energy was estimated to be 3.28 eV for $Ca_{2.95}(VO_4)_2{:}Sm_{0.05}$ [45]. The calculated band gap energy of $Ca_3(VO_4)_2{:}1\%Eu$ was found to be 3.80 eV [46], while Ni constituents decreased the band gap to 2.13 eV for the compositionally close (but Ni-rich) garnet-type $Ca_5Ni_4(VO_4)_6$ compound [39].

In this work, we present the thermostructural properties of $Ca_{10.5-x}Ni_x(VO_4)_7$ (Ni-TCV), based on X-ray powder diffraction results at room and high temperatures (300–1150 K). The high-temperature analysis focused on the impact of Ni content (x) on the thermal expansion behaviour. The effects of substitution on the lattice and electronic structure, and the excited energy relaxation of $Ca_{10.5-x}Ni_x(VO_4)_7$ were also investigated via changes in the absorption and luminescence characteristics in the VUV, UV and visible light ranges.

2. Materials and Methods

Polycrystalline samples of formula $Ca_{10.5-x}Ni_x(VO_4)_7$, with x varying from 0 to 1 (sample named as as S0–S6, see Table 1), were synthesized by solid-state reactions. The samples were prepared using stoichiometric ratios of CaO, NiO (99.99%, Sigma-Aldrich, St. Louis, MO, USA) and V_2O_5 (99%, Prolabo, France). CaO was prepared from $CaCO_3$ (99%, Prolabo) heated in air at 1173 K for a few days. For each composition, 5 g of powder

was weighed, thoroughly mixed, and put in air at 1173 K for about 16 h in a covered alumina crucible. After grinding, pellets were prepared and heated at 1273 K for 16 h, except the first sample ($Ca_{10.34}Ni_{0.16}(VO_4)_7$—S1) which was heated at 1323 K. The compound formation was carried out according to the reaction:

$$(10.5 - x)CaO + 3.5V_2O_5 + xNiO \longrightarrow Ca_{10.5-x}Ni_x(VO_4)_7$$
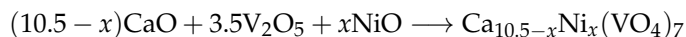
The chemical composition of the crystal was studied using scanning electron microscopy (SEM). The measurements were performed using a JSM-7600F microscope (JEOL, Akishima, Tokyo, Japan). The microscope was equipped with an energy dispersive X-ray (EDX) spectrometer using an X-MaxN 150 Silicon Drift Detector (Oxford Instruments, Abingdon, UK). For the analysis, the surface was coated, using the sputtering method, with a 10 nm thick carbon layer. The measurements were conducted applying a 20 kV accelerating voltage.

Room temperature (RT) X-ray powder diffraction (XRPD) measurements were performed using a Philips X'Pert Pro Alpha1 diffractometer with $CuK\alpha_1$ radiation, in Bragg–Brentano geometry, working in continuous scanning mode, equipped with a linear silicon strip detector and, in RT studies, with an incident beam Ge(111) Johansson monochromator. The idea of utilizing such a detector was first described in [47], whereas the setting of this commercial instrument was reported in [48]. XRPD data were collected at room temperature over the 2θ range of 6°–159.2°, with a step of 0.0167°. Crystal structures were refined using the Rietveld method [49,50] using the Fullprof (version April 2019) software [51].

High-temperature diffraction measurements were conducted using the same diffractometer equipped with an HTK 1200N (Anton Paar, Graz, Austria) temperature stage, in the Bragg–Brentano geometry with $CuK\alpha$ radiation. The high-temperature XRPD data were collected over the 2θ range of 9°–100°. The set temperature range from room temperature (300 K) to 1150 K was selected, with different temperature steps (usually 50 or 100 K). A waiting time was set to 2 min after reaching each temperature step, to stabilize the heater and guarantee uniform temperature within the sample. The high-temperature measurements for $x = 0$ have been performed in [3].

A Carry 5000 UV-Vis-NIR spectrophotometer with a diffuse reflectance accessory (optical integration sphere, DRA 2500) was used to measure diffuse reflection spectra in the 200–850 nm range. Photoluminescence (PL) and luminescence excitation spectra were measured in the 325–850 nm range using a Horiba/Jobin-Yvon Fluorolog 3 spectrofluorometer equipped with various detectors for UV and IR. The PL spectra with UV excitation (120–330 nm) were measured using synchrotron excitation at the PETRA III P66 beamline at Deutsches Elektronen-Synchrotron DESY (Hamburg, Germany). All light reflection and luminescence measurements were performed at room temperature.

Table 1. Structural details of $Ca_{10.5-x}Ni_x(VO_4)_7$ (nominal Ni content, lattice parameters (a, c), volume (V), density (ρ), fractional occupancy of Ni at M5 and reliability factors (R_p and R_{wp})) at room temperature (300(2) K). For all compounds the space group is $R3c$ (Z = 6).

Sample	x			a (Å)	c (Å)	V (Å³)	ρ (g/cm³)	Fractional Occupancy of Ni at M5 Site	R_p	R_{wp}	Ref.
	Nominal	EDX	Rietveld Refinement								
	0		0	10.809(1)	38.028(9)	3847.73	3.17	0	-	-	[1]
	0		0	10.81221(8)	38.02620(3)	3849.840(5)	3.171	0	3.07	4.46	[3]
S0	0		0	10.81388(4)	38.02858(15)	3851.269(25)	3.170	0	3.14	4.26	
S1	0.16	0.16(2)	0.28(3)	10.80110(5)	37.96817(20)	3836.069(33)	3.191	0.104(8)	3.30	4.44	
S2	0.33	0.29(3)	0.39(3)	10.78838(5)	37.89214(21)	3819.375(34)	3.213	0.144(8)	3.33	4.56	
S3	0.5	0.48(2)	0.48(2)	10.77604(6)	37.80589(21)	3801.969(34)	3.237	0.175(8)	2.82	3.95	Present study
S4	0.66	0.66(4)	0.59(2)	10.76527(4)	37.71474(15)	3785.225(25)	3.258	0.214(7)	3.33	4.51	
	0.72(2) [a]			10.7622 [a]	37.6878 [a]	3780.39 [a]					
S5	0.83 [b]	0.71(4)	0.65(2)	10.76219(4)	37.68766(18)	3780.342(28)	3.264	0.237(8)	3.42	4.66	
S6	1 [b]	0.69(2)	0.59(3)	10.76227(6)	37.68802(24)	3780.435(38)	3.264	0.217(10)	3.58	5.34	

[a] value estimated from the V(x) dependence analysis; [b] x = 0.83 and x = 1 refer to the nominal composition of the pellets, while the true Ni content corresponds to the solubility limit.

3. Results and Discussion

3.1. Structure at Room Temperature as a Function of the Ni Content

In order to explore the material elemental composition, the EDX technique was performed (Figure A1). The EDX analysis demonstrates that the Ni content is in line, in the error limit, with the nominal one for all samples of x ranging to 0.66 (see Table 1). For the last two samples, the difference between the Ni content and the nominal value indicates a consistent solubility limit around $x = 0.71(4)$.

The XRPD patterns clearly indicate a whitlockite-related structure with a $R3c$ space group. Sample S5 shows a few extra low-intensity peaks and for S6 these peaks are markedly stronger (see Figure A2), providing further proof that these two samples are out of the solubility range. This impurity in S5 and S6 was identified as $Ca_{2.5}Ni_2(VO_4)_3$ [52], crystallized in a garnet structure.

Rietveld refinements were performed for all samples considering the structure of $Ca_{2.71}Mg_{0.29}(PO_4)_2$ [15], recently named keplerite [16], as the initial model, allowing for the fractional refined occupation of the M5 site by Ni. Similar refinements assuming partial Ni occupation at any of remaining four sites led to considerably higher R factors, therefore such assumptions were rejected.

The refinement procedures followed those described in [6]. The peak shape was determined using the pseudo-Voigt-type function considering two parameters of asymmetry. For oxygen atoms, isotropic displacement factors were set as identical. The minority phase percentage, $Ca_{2.5}Ni_2(VO_4)_3$, increased from 3 wt% (for S5) to 7 wt% (for S6). The obtained garnet-type lattice parameters for $Ca_{2.5}Ni_2(VO_4)_3$ are close to those reported in [52] (a discrepancy is as low as 0.12%). The final refinement results are summarized in Tables 1 and 2. The atomic position results for S5 and S6 were consistent with those of other samples. The final refinement results indicate a whitlockite-β-$Ca_3(PO_4)_2$ structure type (in naming the type, we follow the ICSD database nomenclature [53]) and show strong structural similarity to the samples studied in [6]. The polycrystalline samples have the formula closest to keplerite among the whitlockite-related materials. The quality of the refinements is illustrated for $Ca_{10}Ni_{0.5}(VO_4)_7$ (at 300(2) K) (Figure 2) as a representative example.
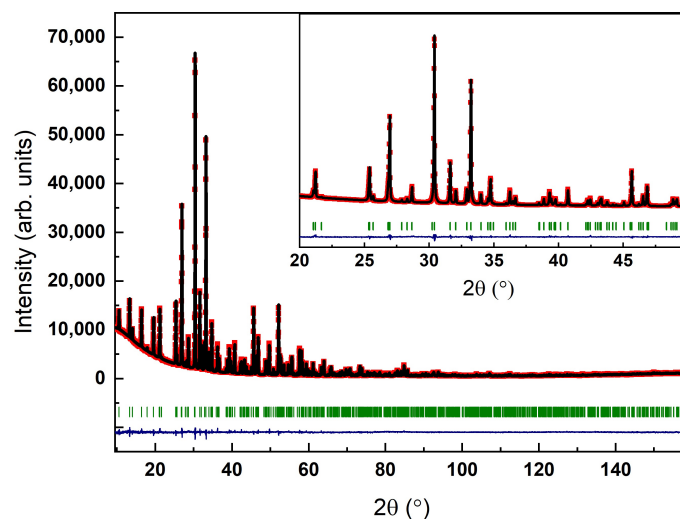
Figure 2. Illustration of the Rietveld refinement result for $Ca_{10}Ni_{0.5}(VO_4)_7$ at 300(2) K. Red squares correspond to experimental data, the black line to the calculated profile, the green vertical bars to the Bragg reflections and the blue line to the difference between the experimental and calculated intensities. The inset presents a magnified view of the 20°–40° refinement region to illustrate its high fitting quality.

Table 2. Results of the structural refinement for $Ca_{10.5-x}Ni_x(VO_4)_7$ within the solubility range.

Site	Wyckoff Position	Coordination	x			
			0.16	**0.33**	**0.5**	**0.66**
M1	18b	x	0.1974(3)	0.1975(3)	0.1993(3)	0.1975(3)
		y	0.3938(3)	0.3944(3)	0.3954(3)	0.3955(3)
		z	0.0028(1)	0.0025(1)	0.0022(1)	0.00275(9)
M2	18b	x	0.1582(3)	0.1590(3)	0.1600(3)	0.1589(3)
		y	0.2808(3)	0.2813(3)	0.2808(3)	0.2805(2)
		z	0.2009(1)	0.20119(11)	0.2014(1)	0.20241(9)
M3	18b	x	0.1873(3)	0.1864(3)	0.1874(3)	0.1860(3)
		y	0.3988(2)	0.3974(2)	0.3973(2)	0.3960(2)
		z	0.1097(1)	0.10983(11)	0.1099(1)	0.11087(9)
M4	6a	x	0	0	0	0
		y	0	0	0	0
		z	0.074(5)	0.0766(5)	0.0749(5)	0.0766(3)
M5	6a	x	0	0	0	0
		y	0	0	0	0
		z	0.2658(2)	0.2655(1)	0.2651(1)	0.2654(1)
V1	6a	x	0	0	0	0
		y	0	0	0	0
		z	0	0	0	0
V2	18b	x	0.3103(2)	0.3109(2)	0.3119(2)	0.3109(2)
		y	0.1371(3)	0.1371(3)	0.1382(3)	0.1378(2)
		z	0.1323(1)	0.1324(1)	0.13213(1)	0.1324(1)
V3	18b	x	0.3484(3)	0.3479(3)	0.3471(3)	0.3466(2)
		y	0.1498(3)	0.1498(3)	0.1483(3)	0.1484(2)
		z	0.2347(1)	0.2350(1)	0.2352(1)	0.2361(1)
O1	6a	x	0.1558(8)	0.1565(8)	0.1542(7)	0.1557(6)
		y	0.0093(10)	0.0106(10)	0.0090(9)	0.0121(8)
		z	0.0123(3)	0.0119(3)	0.0110(3)	0.0121(2)
O2	18b	x	0	0	0	0
		y	0	0	0	0
		z	0.4546(4)	0.4543(4)	0.4550(4)	0.4555(3)
O3	18b	x	0.2683(9)	0.2680(9)	0.2624(9)	0.2565(7)
		y	0.0692(7)	0.0715(7)	0.0689(7)	0.0665(6)
		z	0.0911(2)	0.0911(2)	0.0916(2)	0.09154(19)
O4	18b	x	0.2306(11)	0.2304(11)	0.2320(10)	0.2308(8)
		y	0.2257(10)	0.2256(10)	0.2235(10)	0.2310(8)
		z	0.1446(2)	0.1445(2)	0.1444(2)	0.14583(19)
O5	18b	x	0.2805(10)	0.2818(10)	0.2825(10)	0.2801(8)
		y	−0.0114(9)	−0.0105(8)	−0.0085(8)	−0.0089(7)
		z	0.1561(2)	0.1565(2)	0.1559(2)	0.15765(19)
O6	18b	x	0.0873(10)	0.0857(10)	0.0852(10)	0.0808(8)
		y	0.1843(8)	0.1806(9)	0.1792(8)	0.1722(7)
		z	0.3045(3)	0.3032(3)	0.3022(3)	0.3025(2)
O7	18b	x	0.3998(9)	0.3998(9)	0.3999(8)	0.4006(7)
		y	0.0329(8)	0.0309(8)	0.0308(8)	0.0300(7)
		z	0.2240(3)	0.2246(3)	0.2252(3)	0.2254(2)
O8	18b	x	0.0189(10)	0.0223(9)	0.0225(9)	0.0275(7)
		y	0.2331(10)	0.2357(10)	0.2361(10)	0.2365(8)
		z	0.3804(2)	0.3800(2)	0.3795(2)	0.37923(20)

Table 2. *Cont.*

Site	Wyckoff Position	Coordination	*x*			
			0.16	**0.33**	**0.5**	**0.66**
O9	18b	x	0.1705(8)	0.1701(8)	0.1697(8)	0.1696(7)
		y	0.0762(11)	0.0749(11)	0.0752(11)	0.0717(8)
		z	0.2219(3)	0.2227(3)	0.2249(3)	0.2252(2)
O10	18b	x	0.3752(7)	0.3757(7)	0.3785(7)	0.3788(6)
		y	0.1826(10)	0.1824(10)	0.1831(9)	0.1836(8)
		z	0.2794(2)	0.2797(2)	0.2794(2)	0.27974(19)

3.1.1. Lattice Parameters

The refined lattice parameter *a* decreases from 10.81388(4) Å (sample S0) to 10.76527(4) Å (sample S4), in the same way, the lattice parameter *c* decreases from 38.02858(15) Å to 37.71474(18) Å (Table 1) (Figure 3). The reduction in both lattice parameters *a* and *c*, and consequently the unit cell volume, with increasing Ni clearly proves Ni substitution into the TCV structure. The shrinkage of the lattice is explained by the ionic radii difference of Ca^{2+} and Ni^{2+}. For a six-fold coordination, Ca shows an ionic radius of 1.00 Å, whereas Ni exhibits a considerably smaller radius of 0.69 Å [54]. The observed contradictory trend is consistent with the results previously reported on the substitution of small divalent ions into TCP and TCV, see refs. [6,8,55,56].
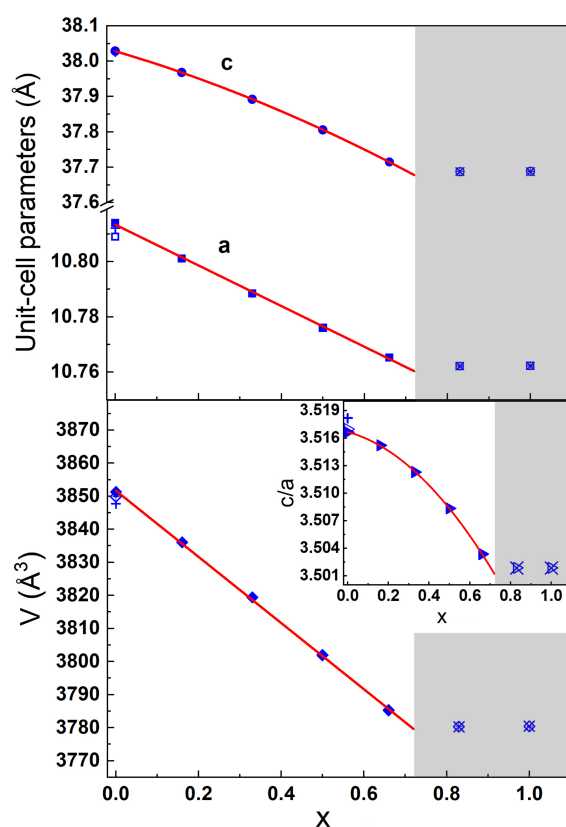
Figure 3. The dependence of the $Ca_{10.5-x}Ni_x(VO_4)_7$ 7 lattice parameters (top), volume (bottom) and axial ratio (*c*/*a*) (inset) (solid symbols; the solid lines are guides to eye) on the nominal Ni content. Two data points at *x* = 0 are taken from the literature (empty symbol from [1] and plus symbol from [3]). The results in the shaded area refer to the samples concluded to be beyond the solubility range (the Ni content in the TCV phase is 0.72(2)).

3.1.2. Solubility Limit

Determining the solubility limit involves analysis of the calculated (i) unit cell size (lattice parameters, unit cell volume and axial ratio), (ii) site occupancies and (iii) interatomic distances. As mentioned above, the ionic sizes of Ca and Ni are markedly different; therefore, the analysis of the unit cell size is expected to provide reliable information when determining the solubility. The difference in the number of electrons is small (20 and 28, respectively). Consequently, using the refined occupancies to determine solubility is less precise, and as a result, this approach was not used here. Naturally, this limit could also be influenced by the synthesis conditions.

The solubility (x_{lim}) limit for several iso-structural orthophosphates has been reported to be $x_{lim} = 1$ or even higher [8,57–59]. For orthovanadates, the known examples refer to doubly substituted compounds, $Ca_{9-x}Mg_xBi(VO_4)_7$ [60] and $Ca_{9-x}Ba_xBi(VO_4)_7$ [61]. Here, both reported x_{lim} values are lower than unity ($x_{lim} = 0.7$), as demonstrated by the phase analysis and the unit cell size. It is notable that the site occupation scheme in doubly substituted compounds is more complex, but the presence of trivalent Bi ions is thought to not alter the occupation by Mg ions, because Bi ions occupy the M1, M2 and M3 sites [60]. In these compounds, Mg and Ba are reported to enter the M5 and M3 sites, respectively. For $Ca_{10.5-x}Ni_x(VO_4)_7$, the secondary phase ($Ca_{2.5}Ni_2(VO_4)_3$) appeared in S5 and S6. Furthermore, no discrepancies were observed in the unit cell size for these two samples when compared to S4. This confirmed that the solid solution limit, x_{lim}, for this compound is between 0.66 and 0.83, the latter resulting from analysis of refined occupancy of M5 site. The solubility limit $x_{lim} = 0.72(2)$ was evaluated from $V(x)$ dependence obtained for the samples prepared by the given synthesis method. This value is in line with results of EDX analysis. The predicted unit cell size data for $x = 0.72$ are listed in Table 1.

3.1.3. Occupancy

Divalent ions with an ionic radius markedly smaller than Ca^{2+}, such as Mn^{2+} [13,62], Co^{2+} [9], Cu^{2+} [63], and Zn^{2+} [55], which are substituted to TCP, were routinely reported to enter the M5 site. Aside from the experimental results, according to the DFT calculations for divalent ions (Mg^{2+}, Zn^{2+}) substituted into the $Ca_3(PO_4)_2$ lattice, divalent ions prefer to enter the M5 site [64,65]. Due to the similar the electronic structures of phosphorus and vanadium substituents, divalent ions were expected to occupy the TCV M5 site. Different sites (M1–M5) for hosting Ni were considered in trial Rietveld refinements. However, according to the best matching model, Ni resides in M5.

3.1.4. Interatomic Distances and Bond Valence Sum Analyses

A further proof of M5 occupancy can be obtained from interatomic distance analysis. The M1 site displays a 7-fold coordination environment and the M1–O average distance is constant at 2.44(1) Å from S0 to S4. The M1–O, M2–O and M3–O distances remain approximately consistent irrespectively of the Ni content (Figure 4 and Table A1). In contrast, for the M5 site, corresponding to the only regular polyhedron, a distance reduction up to about 5.4% is observed from S0 to S4, after which no change in distances is observed at this site. We observe some shortening (up to about 2.7%) of the M4–O distance, but there are no other indications of presence of Ni at M4. This decrease in M5–O length correlates with the presence of Ni^{2+} at this site, possessing a smaller ionic radius compared to Ca^{2+}, strongly supporting M5 as a host for Ni substitution. This is in line with results reported for related compounds. Namely, the distance analyses confirmed the presence of Ni and Cu at M5 for $Ca_{2.9}Me_{0.1}(PO_4)_2$ [13]. Bond length analysis of Mn-substituted $Ca_3(PO_4)_2$ also showed a decrease in M5–O distance [66].
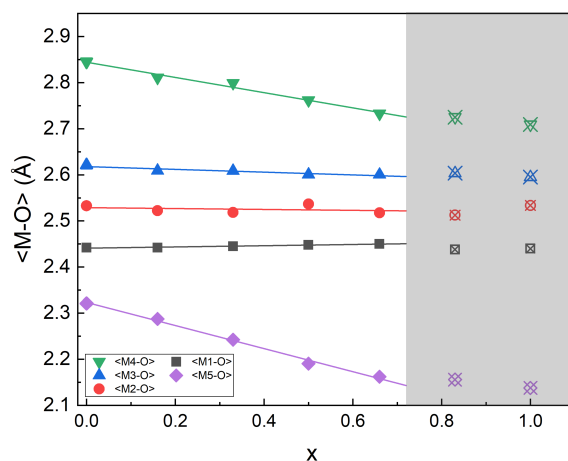
Figure 4. The *x*-dependence of the average interatomic distances of the five Ca sites of $Ca_{10.5-x}Ni_x(VO_4)_7$ (solid symbols; the solid lines are guides to eye) on the nominal Ni content. The results in the shaded area refer to the samples concluded to be beyond the solubility range (the Ni content in the TCV phase is 0.72(2)).

The bond valence sum (BVS) calculations are in good agreement with the expected values from the empirical formula. The value of BVS at M1, M2 and M3 are nearly constant when increasing the Ni content (Table A1). In contrast to the other sites, M4 showed a significantly low BVS value because of the site occupancy factor (the site is half occupied). Conversely, this value for the M5 site changed from 2.03 to 2.25 v.u. The large BVS value for M5 may indicate the presence of Ni in this site, alsoconcluded from the occupancy obtained from the Rietveld refinement. Such a change can be interpreted as described in [13,67,68]. The BVS analysis of $Ca_{2.9}Me_{0.1}(PO_4)_2$ showed large values M5 indicating the presence of Mn, Ni and Cu [13]. A similar analysis for $Ca_9Fe_{0.83}Mg_{0.37}H_{0.37}(PO_4)_7$ and a natural whitlockite specimen indicated a tendency for Fe and Mg to enter the M5 site [67,68].

3.2. Structural Study of $Ca_{10.5-x}Ni_x(VO_4)_7$ in the 300–1150 K Temperature Range

High-temperature measurements were carried out for samples S1–S5 (including the first sample exceeding the solubility limit with an Ni content of 0.72(2)), allowing for the detection of a possible alternative occupation scheme. The *x* = 0 data are taken from [3]. For all samples, the diffraction patterns demonstrate no phase transition or symmetry change from 300 to 1150 K. Due to the increasing temperature, the diffraction peaks shift slightly towards the low-angle side due to continuous lattice expansion. The Rietveld refinement results show that the unit cell volume variation as a function of temperature is smooth but there is an anomaly at around 800–900 K (Figure 5). This anomaly is most visible at the axial ratio $(c/a)(T)$ curve. From 300(2) K to the inflection temperature (T_{inf}), the expansion in the *a* direction is larger compared to the *c* direction, whereas at a temperature exceeding T_{inf}, the lattice parameter *c* increases faster than *a* (this is reflected in the thermal expansion behavior (Figure 6). In other words, for the whole composition range, at that temperature the expansion anisotropy changes its sign. The T_{inf} can be estimated as 905 K for S1 and it decreases to 870 K for S4. Further studies with a finer temperature step should be performed to determine T_{inf} more precisely.

The nature of the above-described anomaly is not fully understood. There have been reports of similar anomalies at high temperatures in structurally related TCV compounds containing mostly trivalent substituents. These anomalies have been observed as phase transitions and symmetry changes ($R3c$ to $R\text{-}3c$) for $Ca_9RE(PO_4)_7$, where RE = In [69], Fe [70], and Eu [71]. Other phase transitions that occur for $Ca_9Yb(VO_4)_7$ and $Ca_8MgEu(PO_4)_7$ include space group changes from $R\text{-}3c$ to $R\text{-}3m$ [72,73]. Such transitions have yet to be observed for divalent substituents, consistent with the findings for Ni-TCV. One hypothesis that could explain the anomaly observed here is that is that at the higher temperatures the Ni ions fractionally migrate to another Ca sites.
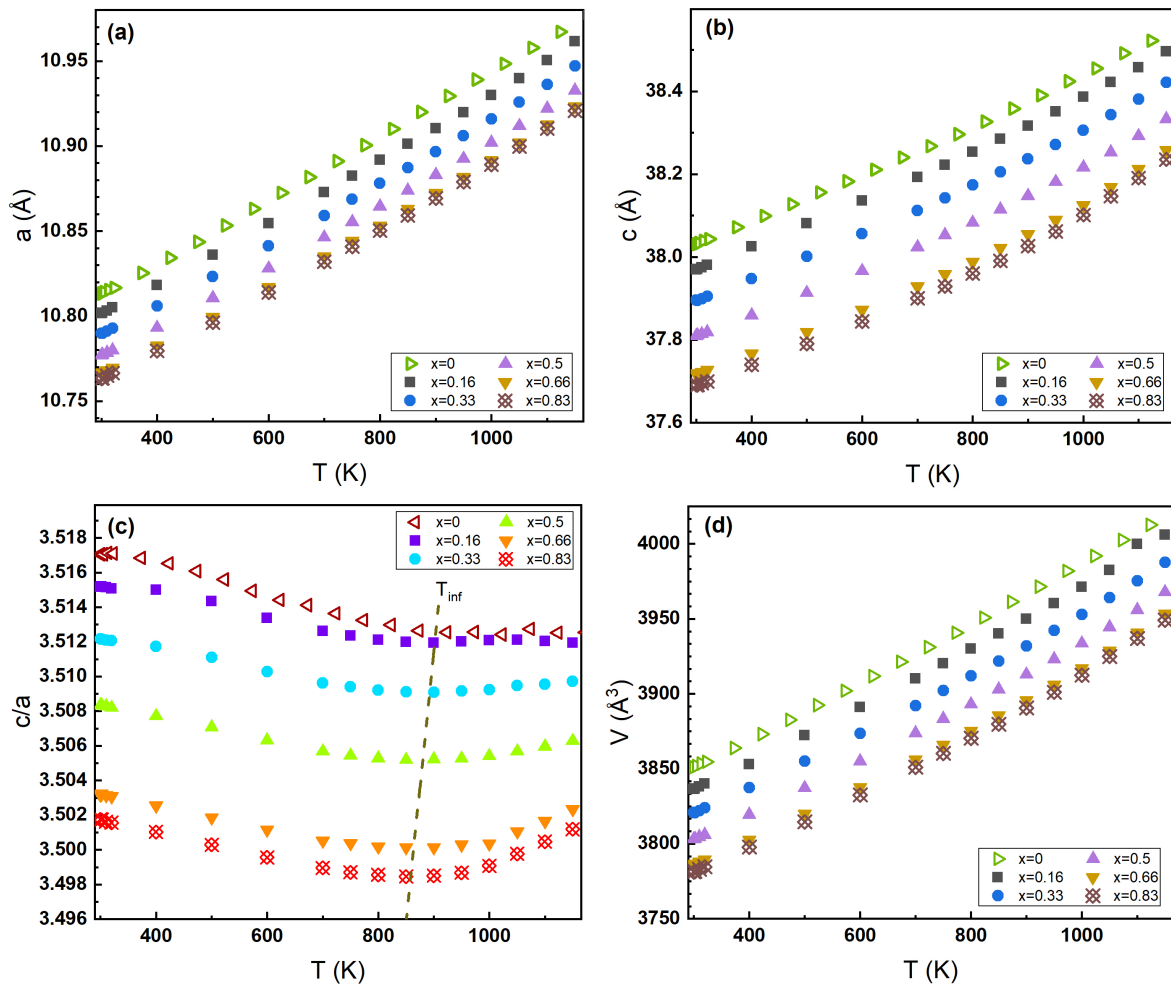
Figure 5. Variation in the lattice parameters (**a**,**b**), axial ratio (**c**) and unit cell volume (**d**) with respect to temperature. Sample with *x* = 0.83 is biphasic and thus out of the solubility limit (the Ni content in the main phase is lower). Data for *x* = 0 is taken from [3]. The dashed line is a guide showing the shift in the inflection temperature with respect to the Ni content.

For many materials, including minerals of various structural complexities, the Laurent polynomial is successfully used to approximate the unit cell size variation with respect to temperature (see, e.g., the review by Fei [74]). This provides a simple analytical description of the thermal expansion coefficient (TEC). If anomalous behaviours in the lattice parameters are observed, then a different description of the variation is required. For Ni-TCV, we applied a combined approach: behaviour below the anomaly is described (I) using a simple model based on the Laurent polynomial, while (II) the Lagrange approach is used for the whole range except the 300 K and 1150 K points.

Results of the TEC variation with respect to temperature are presented in Figure 6. From 300 to 800 K, the temperature dependence of the lattice parameters and volume is well described by Laurent polynomial $y(T) = A + BT + C/T$, similar to other studies for similar temperature ranges [6,75]. A, B and C are fitted coefficients and *y* describes the unit cell size. Variations in the thermal expansion coefficient with respect to temperature for each variable, *y*, were calculated by

$$\alpha_y = \frac{dy(T)}{dT}\frac{1}{y(T)} \tag{1}$$

The Laurent polynomial calculation covers most of the data modelled by the Lagrangian method up to 800 K (Figure 6 and Table 3). Above the inflection temperature, the thermal

expansion of the lattice parameter c sharply increases, influencing the dependence of α_V. The volumetric thermal expansion coefficient for sample $x = 0$ at 300 K is 44.9 MK^{-1} [3], it decreases to 39.24 MK^{-1} for the S4 sample and 38.92 MK^{-1} at the solubility limit. The value obtained for Ca$_{10}$Ni$_{0.5}$(VO$_4$)$_7$ at RT is higher by 7.5% and 12.7% in comparison to Ca$_{10}$Co$_{0.5}$(VO$_4$)$_7$ and Ca$_{10}$Cu$_{0.5}$(VO$_4$)$_7$, respectively [6].
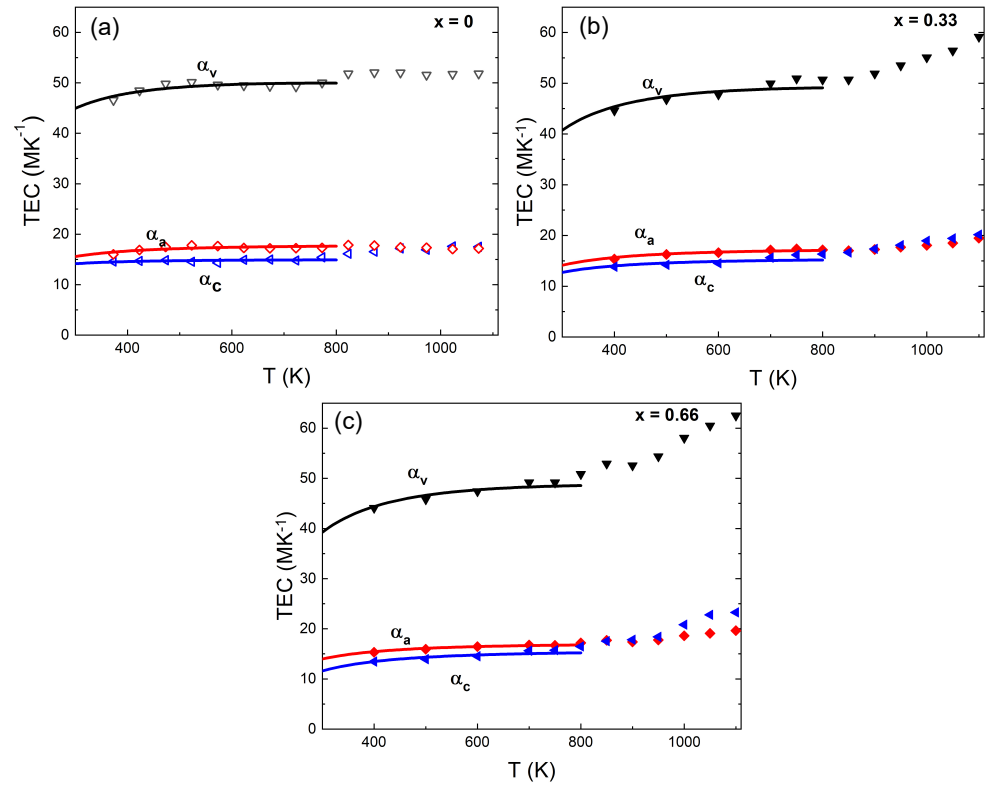
Figure 6. Temperature-dependence of thermal expansion coefficient for the unit cell parameters of Ca$_{10.5-x}$Ni$_x$(VO$_4$)$_7$ ($x = 0$ (**a**), $x = 0.33$(**b**), $x = 0.66$ (**c**)) using both Laurent (solid lines) and Lagrangian interpolation (symbols). The solid line represent the polynomial model. Data for $x = 0$ are taken from [3].

Table 3. Volumetric thermal expansion coefficient of Ca$_{10.5-x}$Ni$_x$(VO$_4$)$_7$ at different temperatures.

	Volumetric Thermal Expansion Coefficient (MK^{-1})				
T (K)			x		
	0.16	**0.33**	**0.5**	**0.66**	**0.83** [a]
300	41.80 [b]	40.73	40.22	39.24	38.92
400	46.58	44.61	44.85	44.08	43.92
	46.44	45.38	44.93	44.37	44.26
500	49.33	46.80	46.35	45.81	45.69
	48.44	47.40	46.97	46.61	46.60
600	48.54	47.77	47.47	47.41	47.48
	49.41	48.37	47.96	47.71	47.75
700	50.03	49.93	48.70	49.16	48.16
	49.88	48.90	48.46	48.27	48.34
750	50.56	50.90	49.22	49.16	49.99
	50.02	49.00	48.60	48.44	48.52
800	51.09	50.69	50.51	50.83	50.32
	50.10	49.09	48.69	48.55	48.63

Table 3. *Cont.*

T (K)	Volumetric Thermal Expansion Coefficient (MK^{-1})				
	x				
	0.16	**0.33**	**0.5**	**0.66**	**0.83** [a]
850	50.78	50.69	50.99	52.91	52.08
900	51.11	51.88	51.76	52.55	54.58
950	53.94	53.48	52.97	54.36	56.13
1000	55.31	55.07	54.06	58.04	60.84
1050	71.15	56.40	56.53	60.47	62.44
1100	58.88	59.11	59.16	62.49	61.82

[a] Sample with x = 0.83 is biphasic and thus out of the solubility limit (the Ni content in the main phase is lower, 0.72(2)). [b] Underlined values are derived from the polynomial function.

A hypothetical source of anomalies in lattice parameter and thermal expansion temperature variations is the process of cation rearrangement with rising temperature. Such anomalies have been reported for other oxides with mixed crystallographic site occupation, such as $Ca_3Eu_2(BO_3)_4$ [76,77]: changes in the cation ordering, namely in the fractional occupation of Eu^{3+} at M1 and M3 was observed above 923 K. The cited results could be obtained due to the use of high quality synchrotron diffraction data.

3.3. Band Gap, Luminescence Behaviour

The absorption spectra $F(\lambda)$ were calculated from the experimentally measured diffuse reflectance spectra $R(\lambda)$ using the well-known and repeatedly tested Kubelka–Munk expression [78]:

$$F = \frac{(1-R)^2}{2R} \tag{2}$$

The reflection spectra used in this calculation are shown in Figure 7. Spectrum 1 represents the previously known absorption spectra of the TCV orthovanadate. Absorption in the wavelength range >400 nm is due to spin-allowed electronic transitions from the ground $^1A_1$ to the excited $^1T_1$ and $^1T_2$ states in the VO_4^{3-} molecular groups [79–81]. Since there are three types of VO_4^{3-} groups in TCV, the energies of the VO_4^{3-} transitions must be different for each of them [46,82], causing a slow increase in the absorption edge in the 350–450 nm range.
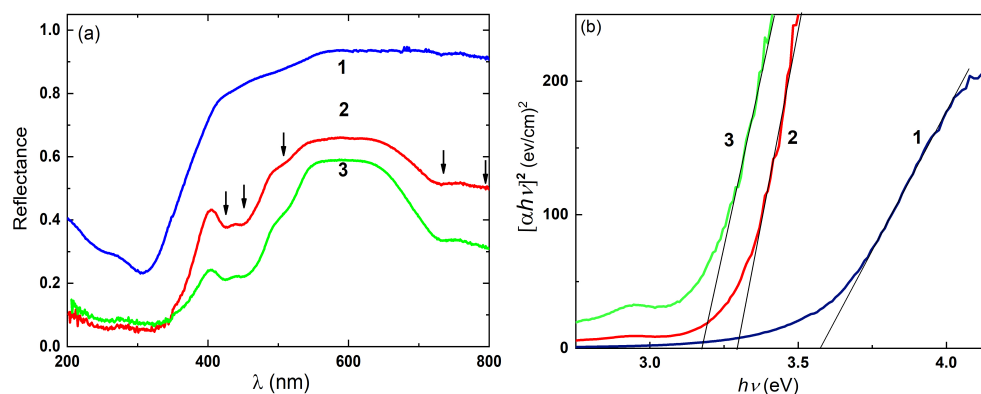

Figure 7. Reflectance spectra (**a**) and Tauc plots (**b**) for the S0 (1- blue curve), S2 (2-red curve), and S4 samples (3-green curve).

Defects and impurities in the crystal lattice have various effects on different types of vanadate groups; therefore, when a nickel dopant is introduced, the shape of the absorption edge changes (Figure 7a, curve 2). In addition, noticeable absorption appears in the 400–550 and 625–800 nm spectral ranges. In the first range, three bands with maxima at 423, 450, and 515 nm are observed, while in the second, two bands appear with maxima at 735

and 800 nm. The peak positions of these bands are marked with arrows in Figure 7a. As the nickel content is increased, the intensity of these absorption bands increases too (Figure 7a, curve 3), indicating their connection with the presence of nickel ions. Referring to the literature data, the aforementioned absorption bands can be assigned to electronic transitions in the Ni^{2+} ions [83–85]. According to the Tanabe–Sugano diagrams, the observed bands in the absorption spectra at 800, 720, 510, 460, and 420 nm can be attributed to electronic transitions from light absorption from the $^3A_2(3F)$ ground state of Ni^{2+} in an octahedral oxygen environment to the $^3T_2(3F)$, $^1T_2(1D)$, and $^3T_1(3P)$ excited states, respectively. Furthermore, two absorption bands at 460 and 420 nm can be attributed to the $^3T_1(3P) \leftarrow {}^3A_2(3F)$ transition [83]. The influence of Ni ions on the crystal lattice is also revealed in the red shift of the optical band gap E_g of the studied compounds. The E_g values were estimated from optical absorption data using the well-known Tauc equation [86]:

$$\alpha_E = A(E - E_g)^n \tag{3}$$

where α is the absorption coefficient, $E = h\nu$, and A is a value considered constant within certain assumptions; while n = 1/2, 3/2, 2, and 3 for direct allowed transitions (n = 1/2), direct forbidden transitions (n = 3/2), indirect allowed transitions (n = 2), and indirect forbidden transitions (n = 3). Considering that there are direct allowed transitions [44,46] (n = 1/2), Equation (3) can be written as:

$$[\alpha(h\nu)h\nu]^2 = A(h\nu - E_g) \tag{4}$$

Now, using $\alpha(h\nu)$ as the above calculated absorption coefficient, $F(h\nu)$, we can plot the dependence of $f(h\nu)$ for the studied samples (Figure 7b):

$$f(h\nu) = [F(h\nu)h\nu]^2 \tag{5}$$

The point of the $f(h\nu)$ intersection with the abscissa determines the optical band gap of the studied material. In particular, we obtained E_g = 3.56 eV for $Ca_3(VO_4)_2$. This value is close to previously reported values using the same optical method (i.e., 3.55 eV) [44].

The introduction of Ni ions into the composition of the compounds leads to a red shift of the E_g value: E_g = 3.29 and 3.16 eV for x = 0.33 and 0.66, respectively. The observed change in E_g is expected, as noted in the introduction, due to the effect of Ni^{2+} on the vanadate band gap. Additionally, it can be said that the band gap for nickel vanadate $Ni_2V_2O_7$ was E_g = 2.15 eV [43]. The decrease in E_g is the result of a stronger deformation of the VO_4^{3-} groups adjacent to the Ni ions. A deformation of the VO_4^{3-} groups under the influence of Ni ions can also be identified by the spectral characteristics of the intrinsic PL of the samples [87,88]. A band of intrinsic PL with a main maximum at 540 nm is observed in the spectra of $Ca_3(VO_4)_2$ in the 350–750 nm range. In addition, at least two more components with maxima at 500 and ~610 nm can be noted in the composition of this band (Figure 8, curve 2). The peak position of these bands is approximately marked with arrows in Figure 8. Such PL is excited by a wide range of UV radiation, from 100 to 350 nm, with a maximum at 308 nm (Figure 9, curve 1). The position of the noted peak in the excitation spectrum coincides with a peak in the $Ca_3(VO_4)_2$ absorption spectrum; therefore, the observed PL is due to VO_4^{3-} group excitation from electronic transitions with absorption $(^1T_1, {}^1T_2) \leftarrow {}^1A_1$. The VO_4^{3-} groups in the studied materials are not ideal tetrahedra, and therefore the decrease in symmetry and the strengthening of the spin–orbit interaction lead to an increase in the probability of transitions with a change of spin <3> ←→ <1>. As a result of the non-radiative relaxation of the energy of the singlet levels $(^1T_1, {}^1T_2)$, low-energy levels of the triplet state $(^3T_1, {}^3T_2)$ are populated, and radiative transitions occur from the ground $^1A_1$ level $(^3T_1, {}^3T_2) \rightarrow {}^1A_1$ [79,81], causing the PL band described above.
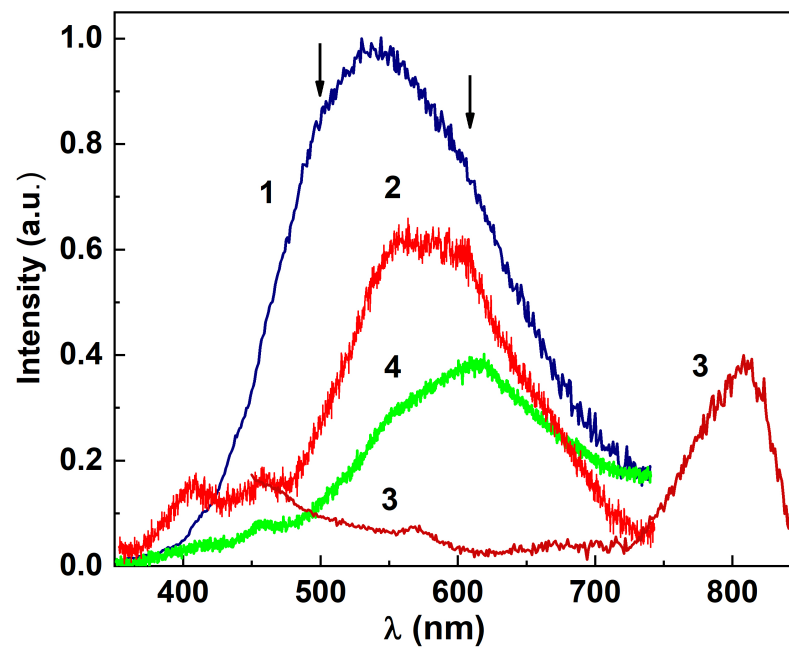
Figure 8. Luminescence spectra of S0 (1), S2 (2, 3), and S4 samples (4); the luminescence excitation wavelengths are 300 (1, 2, 4) and 350 nm (3).
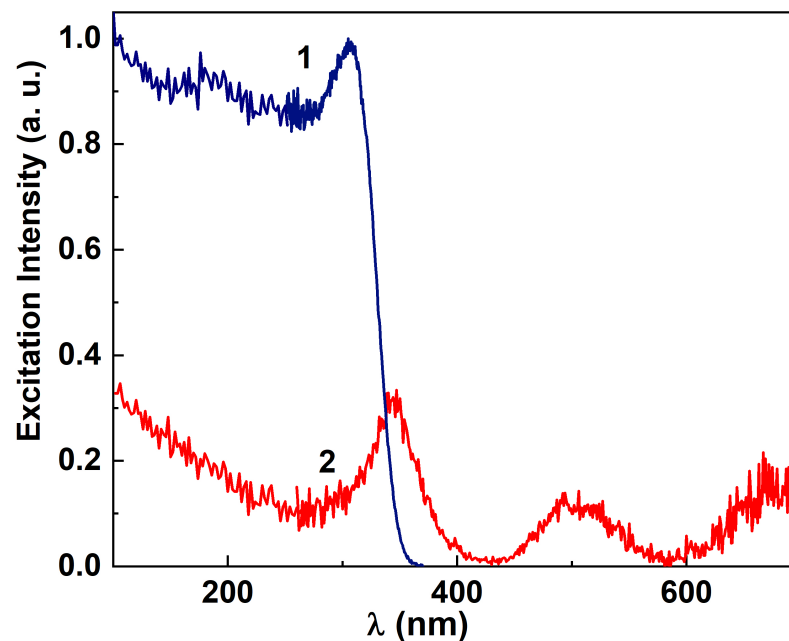
Figure 9. Luminescence excitation spectra for the S0 (1) and S2 samples (2); the luminescence monitoring wavelengths are 540 (curve 1) and 800 nm (curve 2).

The shape of this band changes and the luminescence intensity decreases noticeably when the compounds contain Ni^{2+}. Thus, the spectrum of the sample with $x = 0.33$ is dominated by the luminescence component with a maximum at 540 nm, but the contribution of the 610 nm component noticeably increases (Figure 9, curve 2). By increasing the Ni content ($x = 0.66$), the contribution of this component becomes dominant. Moreover, the contribution of the red shoulder in the 650–725 nm range also increases (Figure 8, curves 2, 3). The described changes in the spectrum profile are associated with the effects of Ni^{2+}, which can be located in different positions (mainly M4 and M5), on neighbouring VO_4^{3-} groups. The observed red shift in the PL spectra correspond to band gap narrowing when the Ni^{2+} concentration increases, while the decrease in the PL intensity is due to a decrease

in the rate of radiation transitions of excited electrons. This behaviour makes Ni-substituted compounds more attractive for applications, particularly, for photocatalysis, especially compounds with high (the highest studied here) Ni content.

In addition, in the PL spectra of samples containing Ni, PL bands were observed at 375–475, 575–700, and 725–850 nm. These bands do not exist in $Ca_3(VO_4)_2$, which exhibits bands at 320–425 nm (excitation maximum at 353 nm), 425–575 (498 nm maximum) and 600–675 nm, with a maximum around 670 nm. It is easy to see that the positions of these PL excitation bands correlate with the bands in the absorption spectra of Ni ions (as discussed above). Therefore, we conclude that the PL bands described above are caused by radiative electronic transitions in Ni ions. These are $^1T_2$ (1D) $\rightarrow$ $^3A_2$(3F) transitions (they cause a green-yellow PL band, 400–525 nm), $^3T_1$(3P) $\rightarrow$ $^3A_2$(3F) (yellow–red PL, 575–700 nm), and $^1T_2$ (1D) $\rightarrow$ $^3T_2$ (3F) (the band of red PL, 700–850 nm) [83,84]. Consequently, the blue-green and yellow-red PL is associated with Ni ions located in the octahedral environment, while tetrahedrally coordinated Ni^{2+} ions do not show PL, or it appears in the blue-green and yellow-red emission bands [84]. Taking into account the fact that the intensity of the red band is ten times higher than the intensity of the short-wavelength luminescence bands, we conclude that the Ni ions in the studied structures mainly occupy octahedrally coordinated positions of M5, consistent with the data of the crystal structure analysis.

4. Conclusions

This study describes the crystal-structure-related properties of a new material, $Ca_{10.5-x}Ni_x(VO_4)_7$, a solid solution at ambient and high temperatures. It also provides basic information on its luminescence properties and band gap. Data on the structure obtained from the Rietveld refinements showed that (1) the solubility limit, x_{lim}, is 0.72(2), with lattice parameters for this composition evaluated as a = 10.7622 Å, c = 37.6878 Å and volume = 3780.39 Å^3; (2) $Ca_{10.5-x}Ni_x(VO_4)_7$ crystallizes in a trigonal structure within the $R3c$ space group, whitlockite-$\beta Ca_3(PO_4)_2$ structure type. Analysis of the occupancies at the available octahedral sites (M1–M5) revealed a preference for Ni ions to occupy the M5 site, consistent with previous findings on similar materials demonstrating a non-random distribution of small divalent ions substituting Ca ions. As a result of the identical site occupancy pattern, the investigated crystals can be regarded as iso-structural with previously reported compounds, such as $Ca_3(VO_4)_2$ with partial substitution of Ca atoms by Mn, Co, or Cu, and keplerite ($Ca_{10.5-x}Mg_x(PO_4)_7$). Further evidence of M5 occupation by Ca and Ni was provided by analysing the interatomic distances and BVS. Lattice parameters and unit cell volume display a smooth variation up to around 800–900 K, with a slight anomaly observed at at temperature of about 850 K. With increasing nickel content, the volumetric thermal expansion at room temperature decreased by about 7%. The observed anomaly was most noticeable in the axial ratio and thermal expansion variations with temperature. Hypothetically, the mentioned anomaly could be attributed to a change in the Ni ion distribution over the different crystallographic sites at higher temperatures.

The optical band gap value decreased from 3.54 eV for the x = 0 sample to 3.16 eV for the x = 0.66 sample. This decrease is significant and suggests that compounds with a high Ni content are potentially useful as photocatalysts. The absorption and photoluminescence spectra indicate that the Ni ions preferentially occupy the M5 site in the TCV structure, consistent with the structural refinement results.

Author Contributions: H.S.R.M., W.P. and R.M. were involved in room and high temperature XRD experiments and data analysis. C.M. was responsible for material synthesis. M.K. was involved in SEM measurements and analysis. O.C., Y.Z. and S.N. were involved in optical experiments and analysis. The original draft was written by H.S.R.M., C.M., S.N. and W.P. helped in reviewing the manuscript. All authors contributed to editing and approved the final version of the manuscript.

Data Availability Statement: The data presented in this study are available on request from the corresponding author.

Appendix A

Linear and volumetric thermal expansion coefficient were evaluated using Lagrange interpolation and subsequently differentiated by the lattice parameter at specific temperatures

$$\alpha_n(T_n) = \left(\frac{T_n - T_{n+1}}{(T_{n-1} - T_n)(T_{n-1} - T_{n+1})} L_{n-1} + \frac{2T_n - T_{n-1} - T_{n+1}}{(T_n - T_{n-1})(T_n - T_{n+1})} L_n \right.$$
$$\left. + \frac{T_n - T_{n-1}}{(T_{n+1} - T_{n-1})(T_{n+1} - T_n)} L_{n+1} \right) \frac{1}{L_n} \tag{A1}$$

where y denotes the lattice parameters (a, c) and the volume (V).

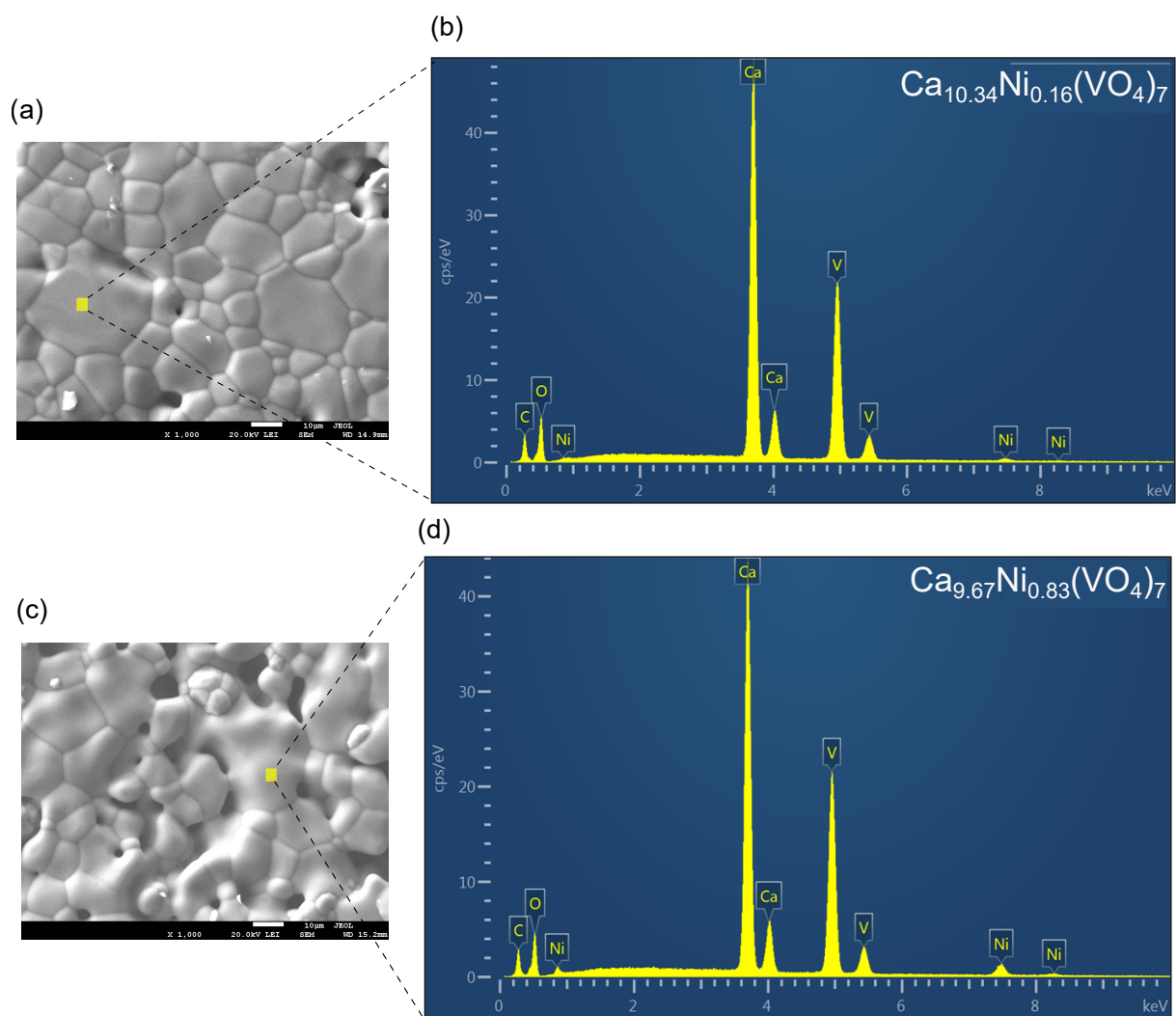**Table A1.** Interatomic distances (with oxygen) and bond valence sum of $Ca_{10.5-x}Ni_x(VO_4)_7$.

Site	\(x\)							
	0.16		**0.33**		**0.5**		**0.66**	
	Interatomic Distances (Å)	BVS (v.u.)	Interatomic Distances (Å)	BVS (v.u.)	Interatomic Distances (Å)	BVS (v.u.)	Interatomic Distances (Å)	BVS (v.u.)
M1–O	2.507(8)		2.517(8)		2.523(8)		2.541(6)	
	2.453(13)		2.438(12)		2.424(13)		2.455(11)	
	2.514(12)		2.52(12)		2.531(12)		2.502(10)	
	2.598(9)	2.02	2.602(9)	2.01	2.592(9)	1.99	2.603(7)	1.99
	2.433(12)		2.456(12)		2.475(12)		2.464(9)	
	2.233(11)		2.246(11)		2.245(11)		2.235(9)	
	2.359(9)		2.338(9)		2.348(9)		2.351(8)	
M2–O	2.372(9)		2.364(9)		2.398(9)		2.381(7)	
	2.476(8)		2.454(8)		2.483(8)		2.471(7)	
	2.45(10)		2.456(10)		2.47(10)		2.418(9)	
	2.369(11)	1.96	2.375(11)	2.01	2.411(11)	1.85	2.369(9)	1.97
	2.795(12)		2.795(12)		2.811(12)		2.793(10)	
	2.852(12)		2.825(11)		2.802(11)		2.82(9)	
	2.415(13)		2.429(13)		2.438(13)		2.462(10)	
	2.450(8)		2.450(8)		2.482(8)		2.426(6)	
M3–O	2.962(11)		2.939(11)		2.905(11)		2.899(8)	
	2.548(3)		2.554(3)		2.555(3)		2.562(3)	
	2.617(7)		2.629(7)		2.620(7)		2.61(6)	
	2.519(12)		2.503(12)		2.517(12)		2.446(10)	
	2.419(9)	1.71	2.421(9)	1.72	2.416(9)	1.76	2.425(8)	1.77
	2.445(12)		2.423(12)		2.396(12)		2.411(9)	
	2.724(10)		2.754(10)		2.776(10)		2.829(9)	
	2.700(8)		2.698(8)		2.663(8)		2.673(7)	
	2.554(12)		2.557(12)		2.557(11)		2.548(10)	
M4–O	2.964(19)		2.946(19)		2.906(19)		2.92(12)	
	2.964(20)		2.946(20)		2.906(19)		2.92(12)	
	2.964(19)		2.946(19)		2.906(19)		2.92(12)	
	2.657(10)	0.33	2.652(10)	0.34	2.617(11)	0.37	2.545(8)	0.42
	2.657(11)		2.652(11)		2.617(11)		2.545(9)	
	2.657(7)		2.652(7)		2.617(8)		2.545(6)	

Table A1. *Cont.*

Site	x							
	0.16		0.33		0.5		0.66	
	Interatomic Distances (Å)	BVS (v.u.)	Interatomic Distances (Å)	BVS (v.u.)	Interatomic Distances (Å)	BVS (v.u.)	Interatomic Distances (Å)	BVS (v.u.)
M5–O	2.264(10) 2.264(11) 2.264(12) 2.311(11) 2.311(3) 2.311(12)	2.03	2.212(10) 2.212(11) 2.212(13) 2.273(11) 2.273(13) 2.273(11)	2.09	2.182(10) 2.182(11) 2.182(12) 2.199(10) 2.199(13) 2.199(11)	2.28	2.129(8) 2.129(8) 2.129(9) 2.196(8) 2.196(9) 2.196(8)	2.25

Figure A1. SEM images of the surface of $Ca_{10.34}Ni_{0.16}(VO_4)_7$ sample (**a**) and $Ca_{9.67}Ni_{0.83}(VO_4)_7$ sample (**c**). The EDX spectrum of the surface of each sample (**b,d**).
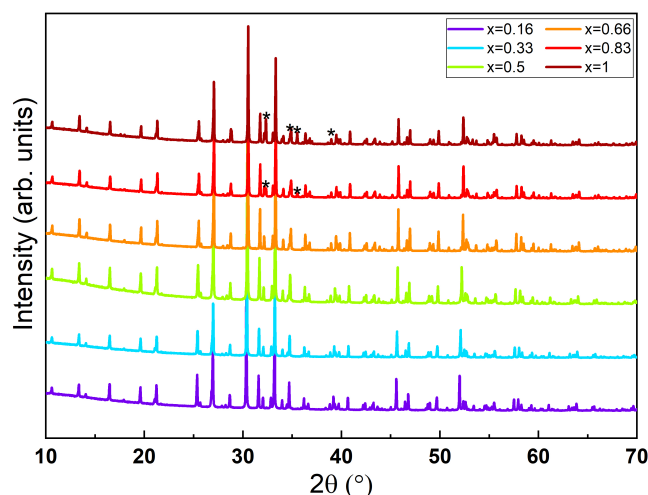
Figure A2. X-ray diffraction pattern of $Ca_{10.5-x}Ni_x(VO_4)_7$ in the limited range $10°–70°$. The black stars in the last two patterns denote $Ca_{2.5}Ni_2(VO_3)_4$ in the second phase.

References

1. Gopal, R.; Calvo, C. The structure of $Ca_3(VO_4)_2$. *Z. Krist.* **1973**, *137*, 67–85. [CrossRef]
2. Grzechnik, A. Crystal structure of $Ca_3(VO_4)_2$ synthesized at 11 GPa and 1373 K. *Solid State Sci.* **2002**, *4*, 523–527. [CrossRef]
3. Sánchez-Martín, J.; Errandonea, D.; Mosafer, H.S.R.; Paszkowicz, W.; Minikayev, R.; Turnbull, R.; Berkowski, M.; Ibáñez-Insa, J.; Popescu, C.; Fitch, A.; et al. The pressure and temperature evolution of the $Ca_2V_2O_8$ crystal structure using powder X-ray diffraction. *CrystEngComm* **2023**, *25*, 1240–1251. [CrossRef]
4. Dickens, B.; Schroeder, L.W.; Brown, W.E. Crystallographic studies of the role of Mg as a stabilizing impurity in β-$Ca_3(PO_4)_2$. The crystal structure of pure β-$Ca_3(PO_4)_2$. *J. Solid State Chem.* **1974**, *10*, 232–248. [CrossRef]
5. Yashima, M.; Sakai, A.; Kamiyama, T.; Hoshikawa, A. Crystal structure analysis of β-tricalcium phosphate $Ca_3(PO_4)_2$ by neutron powder diffraction. *J. Solid State Chem.* **2003**, *175*, 272–277. [CrossRef]
6. Rahimi Mosafer, H.S.; Paszkowicz, W.; Minikayev, R.; Kozłowski, M.; Diduszko, R.; Berkowski, M. The crystal structure and thermal expansion of novel substitutionally disordered $Ca_{10}TM_{0.5}(VO_4)_7$ (TM = Co, Cu) orthovanadates. *Dalt. Trans.* **2021**, *50*, 14762–14773. [CrossRef]
7. Belik, A.A.; Yanov, O.V.; Lazoryak, B.I. Synthesis and crystal structure of $Ca_9Cu_{1.5}(PO_4)_7$ and reinvestigation of $Ca_{9.5}Cu(PO_4)_7$. *Mater. Res. Bull.* **2001**, *36*, 1863–1871. [CrossRef]
8. Spaeth, K.; Goetz-Neunhoeffer, F.; Hurle, K. Cu^{2+} doped β-tricalcium phosphate: Solid solution limit and crystallographic characterization by rietveld refinement. *J. Solid State Chem.* **2020**, *285*, 121225. [CrossRef]
9. Belik, A.; Morozov, V.; Khasanov, S.; Lazoryak, B. Crystal structures of new double calcium and cobalt phosphates. *Mater. Res. Bull.* **1998**, *33*, 987–995. [CrossRef]
10. Legrouri, A.; Romdhane, S.S.; Lenzi, J.; Lenzi, M.; Bonel, G. Influence of preparation method on catalytic properties of mixed calcium-cobalt orthophosphates. *J. Mater. Sci.* **1996**, *31*, 2469–2473. [CrossRef]
11. Zhang, M.; Wu, C.; Li, H.; Yuen, J.; Chang, J.; Xiao, Y. Preparation, characterization and in vitro angiogenic capacity of cobalt substituted β-tricalcium phosphate ceramics. *J. Mater. Chem.* **2012**, *22*, 21686–21694. [CrossRef]
12. Belik, A.A.; Morozov, V.A.; Khasanov, S.S.; Lazoryak, B.I. Crystal structures of new triple $Ca_9CoM(PO_4)_7$ (M = Li, Na, K) phosphates. *Mater. Res. Bull.* **1999**, *34*, 883–893. [CrossRef]
13. Altomare, A.; Corriero, N.; Cuocci, C.; Falcicchio, A.; Moliterni, A.; Rizzi, R. OChemDb: The free online open chemistry database portal for searching and analyzing crystal structure information. *J. Appl. Crystallogr.* **2018**, *51*, 1229–1236. [CrossRef]
14. Kawabata, K.; Yamamoto, T.; Kitada, A. Substitution mechanism of Zn ions in β-tricalcium phosphate. *Phys. B Condens. Matter* **2011**, *406*, 890–894. [CrossRef]
15. Schroeder, L.; Dickens, B.; Brown, W. Crystallographic studies of the role of Mg as a stabilizing impurity in β-$Ca_3(PO_4)_2$. II. Refinement of Mg-containing β-$Ca_3(PO_4)_2$. *J. Solid State Chem.* **1977**, *22*, 253–262. [CrossRef]
16. Britvin, S.N.; Galuskina, I.O.; Vlasenko, N.S.; Vereshchagin, O.S.; Bocharov, V.N.; Krzhizhanovskaya, M.G.; Shilovskikh, V.V.; Galuskin, E.V.; Vapnik, Y.; Obolonskaya, E.V. Keplerite, $Ca_9(Ca_{0.5}\square_{0.5})Mg(PO_4)_7$, a new meteoritic and terrestrial phosphate isomorphous with merrillite, $Ca_9NaMg(PO_4)_7$. *Am. Mineral.* **2021**, *106*, 1917–1927. [CrossRef]
17. Belik, A.A.; Morozov, V.A.; Kotov, R.N.; Khasanov, S.S.; Lazoryak, B.I. Crystal structure of double vanadates $Ca_9R(VO_4)_7$. II. R = Tb, Dy, Ho, and Y. *Crystallogr. Rep.* **2000**, *45*, 389–394. [CrossRef]
18. Fan, J.; Wang, G.; Yuan, F. Growth and characterization of new laser crystal Nd^{3+}:$Ca_{2.85}Gd_{0.1}(VO_4)_2$. *J. Rare Earths* **2012**, *30*, 335–338. [CrossRef]

19. Zhuang, N.; Liu, X.; Xu, Q.; Chen, X.; Zhao, B.; Hu, X.; Chen, J. Crystal growth, nonlinear frequency-doubling and spectral characteristic of Nd:Ca$_9$La(VO$_4$)$_7$ crystal. *J. Alloys Compd.* **2014**, *595*, 113–119. [CrossRef]

20. Zhang, Z.; Loiko, P.; Wu, H.; Mateos, X.; Serres, J.M.; Lin, H.F.; Chen, W.D.; Zhang, G.; Zhang, L.Z.; Díaz, F.; et al. Disordered Tm:Ca$_9$La(VO$_4$)$_7$: A novel crystal with potential for broadband tunable lasing. *Opt. Mater. Express* **2017**, *7*, 484. [CrossRef]

21. Hu, P.N.; Wang, G.F. Growth and spectral properties of Er^{3+}:Ca$_9$La(VO$_4$)$_7$ crystal. *Mater. Res. Innov.* **2011**, *15*, 75–77. [CrossRef]

22. Chen, Z.; Wang, D.; Liu, L.; Yuan, F.; Huang, Y.; Zhang, L.; Lin, Z. Cr^{3+} doped Ca$_3$(VO$_4$)$_2$: A new tunable laser crystal. *J. Alloys Compd.* **2023**, *938*, 168651. [CrossRef]

23. Schrandt, O.; Müller-Buschbaum, H. K$^+$ auf einer mit Ca^{2+} unterbesetzten Punktlage in Ca$_3$(VO$_4$)$_2$: Ein Beitrag über KCa$_{10}$V$_7$O$_{28}$/K$^+$ at an Deficient Ca^{2+} Point Position in Ca$_3$(VO$_4$)$_2$: On KCa$_{10}$V$_7$O$_{28}$. *Zeitschrift für Naturforsch. B* **1996**, *51*, 473–476. [CrossRef]

24. Kosmyna, M.B.; Nazarenko, B.P.; Puzikov, V.M.; Shekhovtsov, A.N.; Paszkowicz, W.; Behrooz, A.; Romanowski, P.; Yasukevich, A.S.; Kuleshov, N.V.; Demesh, M.P.; et al. Ca$_{10}$Li(VO$_4$)$_7$:Nd^{3+}, a promising laser material: Growth, structure and spectral characteristics of a Czochralski-grown single crystal. *J. Cryst. Growth* **2016**, *445*, 101–107. . [CrossRef]

25. Khodasevich, I.A.; Voitikov, S.V.; Orlovich, V.A.; Kosmyna, M.B.; Shekhovtsov, A.N. Raman Spectra of Crystalline Double Calcium Orthovanadates Ca$_{10}$M(VO$_4$)$_7$ (M = Li, K, Na) and Their Interpretation Based on Deconvolution Into Voigt Profiles. *J. Appl. Spectrosc.* **2016**, *83*, 555–561. [CrossRef]

26. Voronina, I.S.; Dunaeva, E.E.; Papashvili, A.G.; Iskhakova, L.D.; Doroshenko, M.E.; Ivleva, L.I. High-temperature diffusion doping as a method of fabrication of Ca$_3$(VO$_4$)$_2$:Mn single crystals. *J. Cryst. Growth* **2021**, *563*, 126104. [CrossRef]

27. Kuz'micheva, G.M.; Ivleva, L.I.; Kaurova, I.A.; Lazarenko, V.A.; Khramov, E.V. Effect of cobalt content on point defects and local structure in activated Ca$_3$(VO$_4$)$_2$ single-crystal solid solutions. *J. Solid State Chem.* **2023**, *318*, 123776. [CrossRef]

28. Glass, A.M.; Abrahams, S.C.; Ballman, A.A.; Loiacono, G. Calcium orthovanadate, Ca$_3$(VO$_4$)$_2$—A new high-temperature ferroelectric. *Ferroelectrics* **1977**, *17*, 579–582. [CrossRef]

29. Bechthold, P.; Liebertz, J.; Deserno, U. Linear and nonlinear optical properties of Ca$_3$(VO$_4$)$_2$. *Opt. Commun.* **1978**, *27*, 393–398. [CrossRef]

30. Matsushima, Y.; Koide, T.; Hiro-Oka, M.; Shida, M.; Sato, A.; Sugiyama, S.; Ito, M. Self-activated vanadate compounds toward realization of rare-earth-free full-color phosphors. *J. Am. Ceram. Soc.* **2015**, *98*, 1236–1244. [CrossRef]

31. Hasegawa, T.; Abe, Y.; Koizumi, A.; Ueda, T.; Toda, K.; Sato, M. Bluish-White Luminescence in Rare-Earth-Free Vanadate Garnet Phosphors: Structural Characterization of LiCa$_3$MV$_3$O$_{12}$ (M = Zn and Mg). *Inorg. Chem.* **2018**, *57*, 857–866. [CrossRef] [PubMed]

32. Chukova, O.V.; Nedilko, S.G.; Slepets, A.A.; Nedilko, S.A.; Voitenko, T.A. Synthesis and Properties of the La$_{1-x-y}$Eu$_y$Ca$_x$VO$_4$ ($0 \leq x, y \leq 0.2$) Compounds. *Nanoscale Res. Lett.* **2017**, *12*, 340. [CrossRef] [PubMed]

33. Chukova, O.; Nedilko, S.A.; Nedilko, S.G.; Voitenko, T.; Slepets, A.; Androulidaki, M.; Papadopoulos, A.; Stratakis, E.; Paszkowicz, W. Strong Eu^{3+} luminescence in La$_{1-x-y}$Er$_{x/2}$Eu$_{x/2}$CayVO$_4$ nanocrystals: The result of co-doping optimization. *J. Lumin.* **2022**, *242*, 118587. [CrossRef]

34. Michalska, M.; Jasiński, J.; Pavlovsky, J.; Żurek-Siworska, P.; Sikora, A.; Gołębiewski, P.; Szysiak, A.; Matejka, V.; Seidlerova, J. Solid state-synthesized lanthanum orthovanadate (LaVO$_4$) Co-doped with Eu as efficient photoluminescent material. *J. Lumin.* **2021**, *233*, 117934. [CrossRef]

35. Zhou, J.; Huang, F.; Xu, J.; Chen, H.; Wang, Y. Luminescence study of a self-activated and rare earth activated Sr$_3$La(VO$_4$)$_3$ phosphor potentially applicable in W-LEDs. *J. Mater. Chem. C* **2015**, *3*, 3023–3028. [CrossRef]

36. Mi, X.; Shi, H.; Wang, Z.; Xie, L.; Zhou, H.; Su, J.; Lin, J. Luminescence properties of M$_3$(VO$_4$)$_2$:Eu^{3+} (M = Ca, Sr, Ba) phosphors. *J. Mater. Sci.* **2016**, *51*, 3545–3554. [CrossRef]

37. Han, L.; Wang, Y.; Zhang, J.; Wang, Y. Enhancement of red emission intensity of Ca$_9$Y(VO$_4$)$_7$:Eu^{3+} phosphor via Bi co-doping for the application to white LEDs. *Mater. Chem. Phys.* **2013**, *139*, 87–91. [CrossRef]

38. Dai, M.; Qiu, K.; Zhang, P.; Zhang, W. Synthesis and luminescence properties of orange–red-emitting Ca$_9$La(VO$_4$)$_7$:Sm^{3+} phosphors co-doped with alkali metal ions. *J. Mater. Sci. Mater. Electron.* **2019**, *30*, 9184–9193. [CrossRef]

39. Lu, Y.; Chen, L.; Huang, Y.; Cheng, H.; Seo, H.J. Photocatalytic ability of vanadate garnet Ca$_5$Ni$_4$(VO$_4$)$_6$ under visible-light irradiation. *J. Phys. D Appl. Phys.* **2015**, *48*, 305107. [CrossRef]

40. Lu, Y.; Pu, Y.; Huang, Y.; Wang, J.; Lu, J. Synthesis, optical properties and photodegradation for methylene blue of Ni-vanadate K$_2$Ni(VO$_3$)$_4$ nanoparticles. *J. Nanopart. Res.* **2015**, *17*, 1–10. [CrossRef]

41. Bhuvaneswari, M.; Selvasekarapandian, S.; Kamishima, O.; Kawamura, J.; Hattori, T. Vibrational analysis of lithium nickel vanadate. *J. Power Sources* **2005**, *139*, 279–283. [CrossRef]

42. Wang, C.; Fang, D.; Wang, H.; Cao, Y.; Xu, W.; Liu, X.; Luo, Z.; Li, G.; Jiang, M.; Xiong, C. Uniform nickel vanadate (Ni$_3$V$_2$O$_8$) nanowire arrays organized by ultrathin nanosheets with enhanced lithium storage properties. *Sci. Rep.* **2016**, *6*, 20826. [CrossRef]

43. Khan, A.Z.; Khan, I.; Sufyan, A.; Anjum, D.; Qurashi, A. Activation of Ni$_2$V$_2$O$_7$ to nonstoichiometric NiV$_3$O$_8$ for solar-driven photoelectrochemical water oxidation. *J. Environ. Chem. Eng.* **2021**, *9*, 105526. [CrossRef]

44. Parhi, P.; Manivannan, V.; Kohli, S.; Mccurdy, P. Synthesis and characterization of M$_3$V$_2$O$_8$ (M = Ca, Sr and Ba) by a solid-state metathesis approach. *Bull. Mater. Sci.* **2008**, *31*, 885–890. [CrossRef]

45. Singh, V.; Seshadri, M.; Pathak, M.S.; Singh, N. Sm 3+ doped calcium orthovanadate Ca$_3$(VO$_4$)$_2$—A spectral study. *Spectrochim. Acta Part A Mol. Biomol. Spectrosc.* **2019**, *217*, 315–321. [CrossRef]

46. Li, L.; Pan, Y.; Wang, W.; Zhang, W.; Wen, Z.; Leng, X.; Wang, Q.; Zhou, L.; Xu, H.; Xia, Q.; et al. O^{2-}-V^{5+} charge transfer band, chemical bond parameters and R/O of Eu^{3+} doped Ca(VO$_3$)$_2$ and Ca$_3$(VO$_4$)$_2$: A comparable study. *J. Alloys Compd.* **2017**, *726*, 121–131. [CrossRef]

47. Zięba, A.; Dąbrowski, W.; Czermak, A. Silicon Strip Detectors and the Prospects of Their Application in X-ray Crystallography. In Proceedings of the First Polish Meeting High-Resolution X-ray Diffractometry and Topography of Conferences Notes, Szklarska Poręba, 14-17 September 1996. (In Polish)

48. Paszkowicz, W. Application of a powder diffractometer equipped with a strip detector and Johansson monochromator to phase analysis and structure refinement. *Nucl. Instrum. Methods Phys. Res. Sect. A Accel. Spectrometers Detect. Assoc. Equip.* **2005**, *551*, 162–177. [CrossRef]

49. Loopstra, B.O.; Rietveld, H.M. The structure of some alkaline-earth metal uranates. *Acta Crystallogr. Sect. B Struct. Crystallogr. Cryst. Chem.* **1969**, *25*, 787–791. [CrossRef]

50. Rietveld, H.M. A profile refinement method for nuclear and magnetic structures. *J. Appl. Crystallogr.* **1969**, *2*, 65–71. [CrossRef]

51. Rodriguez-Carvajal, J. FULLPROF: A program for Rietveld refinement and pattern matching analysis. In Proceedings of the Satellite Meeting on Powder Diffraction of the XV Congress of the IUCr, Toulouse, France, 1990; Volume 127.

52. Wang, N.; He, Z.; Cui, M.; Guo, W.; Zhang, S.; Yang, M.; Tang, Y. Syntheses, structure and magnetic properties of two vanadate garnets Ca$_5$M$_4$V$_6$O$_{24}$ (M = Co, Ni). *J. Solid State Chem.* **2015**, *228*, 245–249. [CrossRef]

53. Inorganic Crystal Structure Database. Available online: https://icsd.fiz-karlsruhe.de/ (accessed on 29 April 2023).

54. Shannon, R.D. Revised effective ionic radii and systematic studies of interatomic distances in halides and chalcogenides. *Acta Crystallogr. Sect. A* **1976**, *32*, 751–767. [CrossRef]

55. Kannan, S.; Goetz-Neunhoeffer, F.; Neubauer, J.; Ferreira, J.M. Synthesis and Structure Refinement of Zinc-Doped β-Tricalcium Phosphate Powders. *J. Am. Ceram. Soc.* **2009**, *92*, 1592–1595. [CrossRef]

56. Enderle, R.; Götz-Neunhoeffer, F.; Göbbels, M.; Müller, F.; Greil, P. Influence of magnesium doping on the phase transformation temperature of β-TCP ceramics examined by Rietveld refinement. *Biomaterials* **2005**, *26*, 3379–3384. [CrossRef] [PubMed]

57. Legrouri, A.; Lenzi, J.; Lenzi, M. Preparation and thermal properties of a series of mixed calcium-cobalt phosphates. *J. Therm. Anal.* **1994**, *41*, 1041–1052. [CrossRef]

58. Leng, Z.; Li, R.; Li, L.; Xue, D.; Zhang, D.; Li, G.; Chen, X.; Zhang, Y. Preferential Neighboring Substitution-Triggered Full Visible Spectrum Emission in Single-Phased Ca$_{10.5-x}$Mg$_x$(PO$_4$)$_7$:Eu^{2+} Phosphors for High Color-Rendering White LEDs. *ACS Appl. Mater. Interfaces* **2018**, *10*, 33322–33334. [CrossRef] [PubMed]

59. Yoshida, K.; Hyuga, H.; Kondo, N.; Kita, H.; Sasaki, M.; Mitamura, M.; Hashimoto, K.; Toda, Y. Substitution model of monovalent (Li, Na, and K), divalent (Mg), and trivalent (Al) metal ions for β-tricalcium phosphate. *J. Am. Ceram. Soc.* **2006**, *89*, 688–690. [CrossRef]

60. Dorbakov, N.G.; Grebenev, V.V.; Titkov, V.V.; Zhukovskaya, E.S.; Stefanovich, S.Y.; Baryshnikova, O.V.; Deyneko, D.V.; Morozov, V.A.; Belik, A.A.; Lazoryak, B.I. Influence of magnesium on dielectric properties of Ca$_{9-x}$Mg$_x$Bi(VO$_4$)$_7$ ceramics. *J. Am. Ceram. Soc.* **2018**, *101*, 4011–4022. [CrossRef]

61. Dorbakov, N.G.; Titkov, V.V.; Stefanovich, S.Y.; Baryshnikova, O.V.; Morozov, V.A.; Belik, A.A.; Lazoryak, B.I. Barium-induced effects on structure and properties of β-Ca$_3$(PO$_4$)$_2$-type Ca$_9$Bi(VO$_4$)$_7$. *J. Alloys Compd.* **2019**, *793*, 56–64. [CrossRef]

62. Fan, J.; Zhou, W.; Luo, J.; Zhang, J.; Wu, Z.c.; Dai, X.; Zhang, X. Efficient and tunable Mn^{2+} sensitized luminescence via energy transfer of a novel red phosphor Ca$_{19}$Mn$_2$(PO$_4$)$_{14}$:Eu^{2+} for white LED. *Ceram. Int.* **2022**, *48*, 15695–15702. [CrossRef]

63. Khan, N.; Morozov, V.A.; Khasanov, S.S.; Lazoryak, B.I. Synthesis and crystal structure of calcium copper phosphate, s-Ca$_{19}$Cu$_2$(PO$_4$)$_{14}$. *Mater. Res. Bull.* **1997**, *32*, 1211–1220. [CrossRef]

64. Debroise, T.; Colombo, E.; Belletti, G.; Vekeman, J.; Su, Y.; Papoular, R.; Hwang, N.S.; Bazin, D.; Daudon, M.; Quaino, P.; et al. One Step Further in the Elucidation of the Crystallographic Structure of Whitlockite. *Cryst. Growth Des.* **2020**, *20*, 2553–2561. [CrossRef]

65. Matsunaga, K.; Kubota, T.; Toyoura, K.; Nakamura, A. First-principles calculations of divalent substitution of Ca^{2+} in tricalcium phosphates. *Acta Biomater.* **2015**, *23*, 329–337. [CrossRef] [PubMed]

66. Mayer, I.; Cohen, S.; Gdalya, S.; Burghaus, O.; Reinen, D. Crystal structure and EPR study of Mn-doped β-tricalcium phosphate. *Mater. Res. Bull.* **2008**, *43*, 447–452. [CrossRef]

67. Deyneko, D.V.; Aksenov, S.M.; Morozov, V.A.; Stefanovich, S.Y.; Dimitrova, O.V.; Barishnikova, O.V.; Lazoryak, B.I. A new hydrogen-containing whitlockite-type phosphate Ca$_9$(Fe$_{0.63}$ Mg$_{0.37}$)H$_{0.37}$(PO$_4$)$_7$: Hydrothermal synthesis and structure. *Z. Krist. Cryst. Mater.* **2014**, *229*, 823–830. [CrossRef]

68. Capitelli, F.; Bosi, F.; Capelli, S.C.; Radica, F.; Ventura, G.D. Neutron and xrd single-crystal diffraction study and vibrational properties of whitlockite, the natural counterpart of synthetic tricalcium phosphate. *Crystals* **2021**, *11*, 225. [CrossRef]

69. Morozov, V.A.; Belik, A.A.; Stefanovich, S.Y.; Grebenev, V.V.; Lebedev, O.I.; Van Tendeloo, G.; Lazoryak, B.I. High-temperature phase transition in the whitlockite-type phosphate Ca$_9$In(PO$_4$)$_7$. *J. Solid State Chem.* **2002**, *165*, 278–288. [CrossRef]

70. Lazoryak, B.I.; Morozov, V.A.; Belik, A.A.; Stefanovich, S.Y.; Grebenev, V.V.; Leonidov, I.A.; Mitberg, E.B.; Davydov, S.A.; Lebedev, O.I.; Van Tendeloo, G. Ferroelectric phase transition in the whitlockite-type Ca$_9$Fe(PO$_4$)$_7$; Crystal structure of the paraelectric phase at 923 K. *Solid State Sci.* **2004**, *6*, 185–195. [CrossRef]

71. Benhamou, R.A.; Bessière, A.; Wallez, G.; Viana, B.; Elaatmani, M.; Daoud, M.; Zegzouti, A. New insight in the structure–luminescence relationships of Ca$_9$Eu(PO$_4$)$_7$. *J. Solid State Chem.* **2009**, *182*, 2319–2325. [CrossRef]

72. Lazoryak, B.I.; Aksenov, S.M.; Stefanovich, S.Y.; Dorbakov, N.G.; Belov, D.A.; Baryshnikova, O.V.; Morozov, V.A.; Manylov, M.S.; Lin, Z. Ferroelectric crystal $Ca_9Yb(VO_4)_7$ in the series of $Ca_9R(VO_4)_7$ non-linear optical materials (R = REE, Bi, Y). *J. Mater. Chem. C* **2017**, *5*, 2301–2310. [CrossRef]

73. Belik, A.A.; Morozov, V.A.; Deyneko, D.V.; Savon, A.E.; Baryshnikova, O.V.; Zhukovskaya, E.S.; Dorbakov, N.G.; Katsuya, Y.; Tanaka, M.; Stefanovich, S.Y.; et al. Antiferroelectric properties and site occupations of R3+cations in Ca8MgR(PO4)7luminescent host materials. *J. Alloys Compd.* **2017**, *699*, 928–937. [CrossRef]

74. Fei, Y. Thermal Expansion. In *Mineral Physics & Crystallography: A Handbook of Physical Constants*; Ahrens, T.J., Ed.; American Geophysical Union: Washington, DC, USA, 1995; Volume 2, pp. 29–44. [CrossRef]

75. Paszkowicz, W.; Shekhovtsov, A.; Kosmyna, M.; Loiko, P.; Vilejshikova, E.; Minikayev, R.; Romanowski, P.; Wierzchowski, W.; Wieteska, K.; Paulmann, C.; et al. Structure and thermal expansion of$Ca_9Gd(VO_4)_7$: A combined powder-diffraction and dilatometric study of a Czochralski-grown crystal. *Nucl. Instrum. Meth. Phys. Res. Sect. B Beam Interact. Matt Atoms* **2017**, *411*, 100–111. [CrossRef]

76. Kosyl, K.M.; Paszkowicz, W.; Shekhovtsov, A.N.; Kosmyna, M.B.; Antonowicz, J.; Olczak, A.; Fitch, A.N. Variation of cation distribution with temperature and its consequences on thermal expansion for $Ca_3Eu_2(BO_3)_4$. *Acta Crystallogr. Sect. B Struct. Sci. Cryst. Eng. Mater.* **2020**, *76*, 554–562. [CrossRef]

77. Kosyl, K. Structure and Disorder in Rare Earth Borates $Ca_3RE_2(BO_3)_4$: Diffraction Studies under Ambient Conditions and as a Function of Temperature. Ph.D. Thesis, Polish Academy of Sciences, Warsaw, Poland, 2022.

78. Kubelka, P. New Contributions to the Optics of Intensely Light-Scattering Materials. Part II: Nonhomogeneous Layers. *J. Opt. Soc. Am.* **1954**, *44*, 330–335. [CrossRef]

79. Ronde, H.; Blasse, G. The nature of the electronic transitions of the vanadate group. *J. Inorg. Nucl. Chem.* **1978**, *40*, 215–219. [CrossRef]

80. Nakajima, T.; Isobe, M.; Tsuchiya, T.; Ueda, Y.; Kumagai, T. A revisit of photoluminescence property for vanadate oxides AVO_3 (A:K, Rb and Cs) and $M_3V_2O_8$ (M:Mg and Zn). *J. Lumin.* **2009**, *129*, 1598–1601. [CrossRef]

81. Nakajima, T.; Isobe, M.; Tsuchiya, T.; Ueda, Y.; Manabe, T. Correlation between luminescence quantum efficiency and structural properties of vanadate phosphors with chained, dimerized, and isolated VO_4 tetrahedra. *J. Phys. Chem. C* **2010**, *114*, 5160–5167. [CrossRef]

82. Min, X.; Huang, Z.; Fang, M.; Liu, Y.; Tang, C.; Wu, X. Luminescence properties of self-activated $M_3(VO_4)_2$ (M = Mg, Ca, Sr, and Ba) phosphors synthesized by solid-state reaction method. *J. Nanosci. Nanotechnol.* **2016**, *16*, 3684–3689. [CrossRef]

83. Zannoni, E.; Cavalli, E.; Toncelli, A.; Tonelli, M.; Bettinelli, M. Optical spectroscopy of $Ca_3Sc_2Ge_3O_{12}:Ni^{2+}$. *J. Phys. Chem. Solids* **1999**, *60*, 449–455. [CrossRef]

84. Wang, S.F.; Gu, F.; Lü, M.K.; Song, C.F.; Xu, D.; Yuan, D.R.; Liu, S.W. Photoluminescence of sol–gel derived $ZnTiO_3:Ni^{2+}$ nanocrystals. *Chem. Phys. Lett.* **2003**, *373*, 223–227. [CrossRef]

85. Ravikumar, R.V.; Chandrasekhar, A.V.; Ramamoorthy, L.; Reddy, B.J.; Reddy, Y.P.; Yamauchi, J.; Rao, P.S. Spectroscopic studies of transition metal doped sodium phosphate glasses. *J. Alloys Compd.* **2004**, *364*, 176–179. [CrossRef]

86. Tauc, J.; Grigorovici, R.; Vancu, A. Optical properties and electronic structure of amorphous germanium. *Phys. Status Solidi* **1966**, *15*, 627–637. [CrossRef]

87. Li, L.; Liu, X.G.; Noh, H.M.; Jeong, J.H. Chemical bond parameters and photoluminescence of a natural-white-light $Ca_9La(VO_4)_7:Tm^{3+}$, Eu^{3+} with one $O^{2-} \rightarrow V^{5+}$ charge transfer and dual f-f transition emission centers. *J. Solid State Chem.* **2015**, *221*, 95–101. [CrossRef]

88. Luo, Y.; Xia, Z.; Lei, B.; Liu, Y. Structural and luminescence properties of Sr_2VO_4Cland $Sr_5(VO_4)_3$Cl: Self-activated luminescence and unusual Eu^{3+} emission. *RSC Adv.* **2013**, *3*, 22206–22212. [CrossRef]